Progress In Electromagnetics Research M, Vol. 57, 139–149, 2017

Orthogonal Radiation Field Construction for Microwave Staring Correlated Imaging

Bo Liu* **and Dongjin Wang**

Abstract—Microwave staring correlated imaging (MSCI) achieves high resolution imaging results by employing the temporal-spatial independent radiation field. In MSCI, the imaging performance is determined by the independent degree of the radiation field. In this paper, a novel kind of ideal independent radiation field named the orthogonal radiation field (ORF) is constructed for MSCI. Firstly, a group of two-dimensional (2-D) orthogonal basis functions are used to construct the ideal ORF samples. Then a method is proposed to construct the ORF samples by designing the transmitting signals. The numerical simulations validate the feasibility of this method. Finally, when the ORF is applied in MSCI, the numerical simulations achieve high resolution imaging results and demonstrate good imaging performance that is robust to noise.

1. INTRODUCTION

Microwave staring correlated imaging (MSCI) is a newly proposed high resolution microwave imaging technique [1–3]. The essential principle of MSCI is to construct the temporal-spatial independent radiation field in the imaging region, to make scatters located at different positions reflect independent radiation field from each other, and then to reconstruct the target image by utilizing the echo signals and the known radiation field samples.

The key idea of MSCI is to construct the temporal-spatial independent radiation field. In recent years, several methods have been studied to construct the temporal-spatial independent radiation field. Using the random modulated signals to construct the field is the most common method, such as the pseudo-random gold sequence is utilized in [1, 2], the signals modulated with zero-mean Gaussian noise upon frequency, amplitude, and phase respectively are used in [3–5], the band-pass white Gaussian noise is used in [6, 7], and random frequency hopping signals are used in [8]. Moreover, the effect of array geometry on imaging performance is analyzed based on the effective rank theory, and useful design guidance about the array geometry is obtained [9]. In [10], the plasma lens array is used to modulate the azimuth wavefront. In [11, 12], the complex radiation patterns are generated by the mode-mixing cavity and printed aperiodic cavity respectively. In [13, 14], metamaterials enable the design of a planar antenna that illuminates a scene with dramatically varying radiation patterns as function of frequency. In MSCI, the SNR is generally required to be not less than 20 dB by employing the radiation field constructed by the existing methods, that means the imaging model is sensitive to noise. Therefore, the independent degree of the radiation field still needs to be improved.

In this paper, we focus on the construction of temporal-spatial independent radiation field and construct a novel kind of ideal independent radiation field, which is named the orthogonal radiation field. Firstly, we use a group of 2-D orthogonal basis functions to construct the ideal ORF samples. This is a significant difference from the existing methods. It ensures the high independent degree between

Received 20 April 2017, Accepted 2 June 2017, Scheduled 12 June 2017
* Corresponding author: Bo Liu (bliu@mail.ustc.edu.cn).
The authors are with the Key Laboratory of Electromagnetic Space Information, Chinese Academy of Sciences, University of Science and Technology of China, Hefei, Anhui 230026, China.

the radiation field samples. Then the ideal ORF samples are approximated by properly designing the transmitting signals. Suppose that each signal is made up of N known frequencies, and the signal is determined when the complex amplitude of each frequency is obtained. The details of this method are described in Section 3. Finally, when the approximated ORF samples are applied in MSCI, high resolution imaging results with good robustness to noise are obtained.

The rest of this paper is organized as follows. In Section 2, the imaging model of MSCI is established. The details of the ORF construction are presented in Section 3. In Section 4, the numerical simulations are presented, and we make a concluding remark in Section 5 to summarize this paper.

2. MICROWAVE STARING CORRELATED IMAGING MODEL

The geometry of MSCI system is illustrated in Figure 1. There is an array of M transmitting elements and a receiving element. Let (x, y, z) be Cartesian coordinates with the origin O. The array aperture is labeled as D, and the 2-D imaging region is labeled as S. $\mathbf{r}'_m$, $\mathbf{r}''_0$ and $\mathbf{r}$ is the position vector of m-th transmitting element, the receiving element and an arbitrary point within S, respectively.

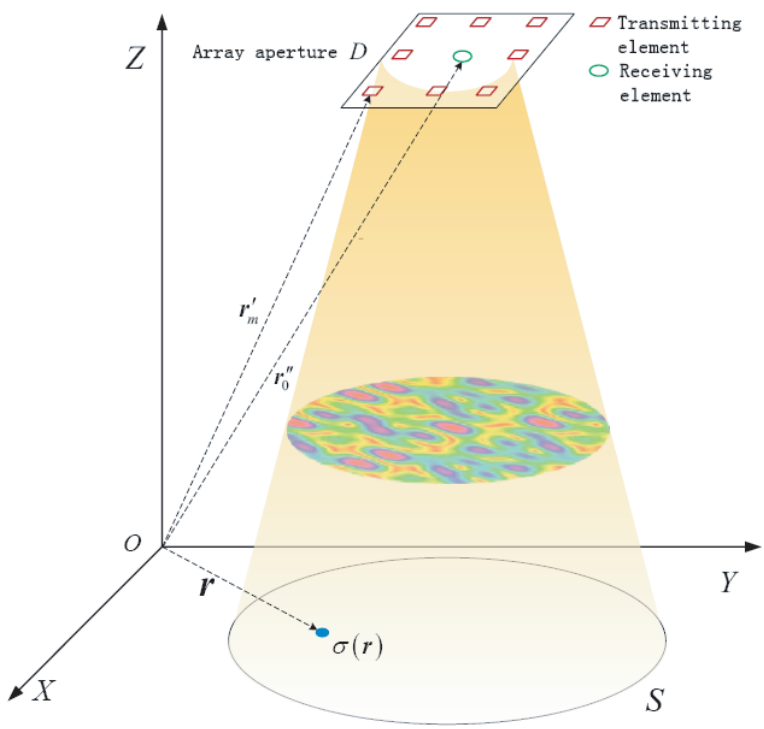

Figure 1. The geometry of MSCI.

The radiation field $E_i(\mathbf{r}, t)$ generated by the M transmitting elements can be expressed as [1]

$$E_i(\mathbf{r},t) = \sum_{m=1}^{M} \int_{D_m} \frac{1}{4\pi|\mathbf{r}-\mathbf{r}'|} A_m(\mathbf{r}') f_m\left(t - \frac{|\mathbf{r}-\mathbf{r}'|}{c}\right) d\mathbf{r}' \tag{1}$$

where c denotes the speed of light, D_m the sub-aperture of the m-th transmitting element, $f_m(t)$ the signal of the m-th transmitting element, and $A_m(\mathbf{r}')$ the amplitude of the source in the sub-aperture D_m.

The received echo signal $s_r(t)$ of the target in the imaging region can be expressed as follows

$$s_r(t) = \int_S \frac{1}{4\pi|\mathbf{r}-\mathbf{r}''_0|} E_i\left(\mathbf{r}, t - \frac{|\mathbf{r}-\mathbf{r}''_0|}{c}\right) \sigma(\mathbf{r}) d\mathbf{r} + n(t) \tag{2}$$

where $\sigma(\mathbf{r})$ denotes the backscattering coefficient distribution of the target in the imaging region, and the $n(t)$ denotes the addictive noise. We define the modified radiation field $E_r(\mathbf{r},t)$ as

$$E_r\left(\mathbf{r},t\right) = \frac{1}{4\pi|\mathbf{r}-\mathbf{r}_0''|} E_i\left(\mathbf{r}, t - \frac{|\mathbf{r}-\mathbf{r}_0''|}{c}\right) \tag{3}$$

Unless otherwise explicitly stated, the radiation field refers to $E_r(\mathbf{r},t)$ in the rest of this paper. Therefore, the received echo signal can be written as

$$s_r\left(t\right) = \int\limits_S E_r\left(\mathbf{r},t\right)\sigma(\mathbf{r})d\mathbf{r} + n\left(t\right) \tag{4}$$

According to Eq. (4), the time domain is discretized as $\{t_1, t_2, \ldots, t_k, \ldots, t_K\}$ and the imaging region discretized as $\{\mathbf{r}_1, \mathbf{r}_2, \ldots, \mathbf{r}_l, \ldots, \mathbf{r}_L\}$, and $\mathbf{r}_l$ is the position vector of the l-th imaging cell center. The imaging region is divided into L imaging cells according to the minimum unit to be resolved. Let $\sigma_l = \sigma(\mathbf{r}_l)$ stand for the scattering feature of the l-th imaging cell. The scattering coefficient vector is expressed as

$$\boldsymbol{\sigma} = [\sigma_1, \sigma_2, \ldots, \sigma_l, \ldots \sigma_L]^T \tag{5}$$

Therefore, the imaging model for MSCI can be described as a following matrix equation

$$\mathbf{s}_r = \mathbf{E}_r \cdot \boldsymbol{\sigma} + \mathbf{n} \tag{6}$$

where $\mathbf{s}_r = [s_r(t_1), s_r(t_2), \ldots, s_r(t_K)]^T$ represents echo signal vector, $\mathbf{n} = [n(t_1), n(t_2), \ldots, n(t_K)]$ represents the noise vector, and $\mathbf{E}_r$ denotes the imaging matrix as

$$\mathbf{E}_r = \begin{bmatrix} E_r\left(\mathbf{r}_1, t_1\right) & E_r\left(\mathbf{r}_2, t_1\right) & \ldots & E_r\left(\mathbf{r}_L, t_1\right) \\ E_r\left(\mathbf{r}_1, t_2\right) & E_r\left(\mathbf{r}_2, t_2\right) & \ldots & E_r\left(\mathbf{r}_L, t_2\right) \\ \vdots & \vdots & \ddots & \vdots \\ E_r\left(\mathbf{r}_1, t_K\right) & E_r\left(\mathbf{r}_2, t_K\right) & \ldots & E_r\left(\mathbf{r}_L, t_K\right) \end{bmatrix} \tag{7}$$

When the imaging matrix is full rank, namely $rank(\mathbf{E}_r) = L$, Equation (3) has a unique solution. However, if the independent degree between the radiation samples is not high, it will make the imaging matrix $\mathbf{E}_r$ ill-conditioned. And the imaging model in Eq. (6) will be very sensitive to noise. According to Eq. (7), the row vector of the imaging matrix is obtained by discretization of the radiation field at the sampling time. Thus, the row rank of $\mathbf{E}_r$ relies on the independent degree of radiation field at different sampling times. Therefore, how to construct the radiation field samples with high independent degree is a key problem of MSCI. Focusing on this problem, this paper constructs a novel kind of ideal independent radiation field, which is named the orthogonal radiation field.

3. ORTHOGONAL RADIATION FIELD CONSTRUCTION

Assuming that $E_r(\mathbf{r}, t_{k_1})$ and $E_r(\mathbf{r}, t_{k_2})$ are two radiation field samples. The inner product $\Gamma(t_{k_1}, t_{k_2})$ of the two samples is given by

$$\Gamma\left(t_{k_1}, t_{k_2}\right) = \int\limits_S E_r\left(\mathbf{r}, t_{k_1}\right) \cdot E_r\left(\mathbf{r}, t_{k_2}\right)^* d\mathbf{r} \tag{8}$$

If $\Gamma(t_{k_1}, t_{k_2}) = 0$, when $t_{k_1} \neq t_{k_2}$, the two radiation field samples are termed to be orthogonal to each other. According to this definition, the radiation field samples of any two different sampling times are orthogonal. Thus, it ensures that the row rank of the imaging matrix is equal to the radiation field samples when $K \leq L$. More significantly, it makes the row vectors of the imaging matrix are orthogonal to each other.

In this paper, the construction of ORF consists of two steps. Firstly, we choose a group of 2-D orthogonal basis functions as ideal ORF samples. And then the ideal ORF samples are approximated by properly designing the signals of the transmitting elements.

There are many kinds of 2-D orthogonal basis functions. The general form of a group of orthogonal basis functions can be expressed as

$$\{\Psi_1(\mathbf{r}), \Psi_2(\mathbf{r}), \ldots, \Psi_k(\mathbf{r}), \ldots\}, \mathbf{r} \in S \tag{9}$$

where $\Psi_k(\mathbf{r})$ is considered as the ideal ORF sample that $E_r(\mathbf{r}, t_k)$ is going to approximate.

Assuming that $E_r(\mathbf{r}, t_k) = \Psi_k(\mathbf{r})$, substitute Eq. (1) to Eq. (3), then $\Psi_k(\mathbf{r})$ can be expressed as

$$\Psi_k(\mathbf{r}) = \frac{1}{(4\pi)^2 |\mathbf{r} - \mathbf{r}_0''|} \sum_{m=1}^{M} \int_{D_m} \frac{1}{|\mathbf{r} - \mathbf{r}'|} A_m(\mathbf{r}') f_m(t_k - \frac{|\mathbf{r} - \mathbf{r}'|}{c} - \frac{|\mathbf{r} - \mathbf{r}_0''|}{c}) d\mathbf{r}' \tag{10}$$

Assume that $F_m(\omega)$ is the Fourier transform result of $f_m(t)$, and it is known that the spectrum range of this signal is ω_L to ω_H. Thus $f_m(t)$ can be expressed as

$$f_m(t) = \frac{1}{2\pi} \int_{\omega_L}^{\omega_H} F_m(\omega) e^{j\omega t} d\omega \tag{11}$$

Further, the spectral domain is discretized as $\{\omega_1, \omega_2, \ldots, \omega_n, \ldots, \omega_N\}$, and ω_n is

$$\omega_n = \omega_L + (n-1) \cdot \Delta\omega \tag{12}$$

where $\Delta\omega = (\omega_H - \omega_L)/N$. Thus $f_m(t)$ can be written as

$$f_m(t) = \frac{\Delta\omega}{2\pi} \sum_{n=1}^{N} F_m(\omega_n) e^{j\omega_n t} \tag{13}$$

According to Eq. (13), if we calculate the value of $F_m(\omega_n)$, the signal $f_m(t)$ can be determined. Substituting Eq. (13) to Eq. (10), we can obtain

$$\Psi_k(\mathbf{r}) = \sum_{m=1}^{M} \sum_{n=1}^{N} \Phi_{m,n}(\mathbf{r}, t_k) F_m(\omega_n) \tag{14}$$

where

$$\Phi_{m,n}(\mathbf{r}, t_k) = \frac{\Delta\omega}{32\pi^3 |\mathbf{r} - \mathbf{r}_0''|} \int_{D_m} \frac{1}{|\mathbf{r} - \mathbf{r}'|} A_m(\mathbf{r}') e^{j\omega_n \left(t_k - \frac{|\mathbf{r} - \mathbf{r}'|}{c} - \frac{|\mathbf{r} - \mathbf{r}_0''|}{c}\right)} d\mathbf{r}' \tag{15}$$

In Eq. (14), $\mathbf{r}$ is discretized as $\{\mathbf{r}_1, \mathbf{r}_2, \ldots, \mathbf{r}_q, \ldots, \mathbf{r}_Q\}$. And the radiation field values at these points are arranged into a vector as

$$\mathbf{e}_{rk} = [\Psi_k(\mathbf{r}_1), \Psi_k(\mathbf{r}_2), \ldots, \Psi_k(\mathbf{r}_q), \ldots, \Psi_k(\mathbf{r}_Q)]^T \tag{16}$$

Therefore, Eq. (14) can be described as the following matrix equation

$$\mathbf{e}_{rk} = \mathbf{\Phi}_k \cdot \mathbf{F} \tag{17}$$

where,

$$\mathbf{\Phi}_k = \begin{bmatrix} \Phi_{1,1}(\mathbf{r}_1, t_k) & \Phi_{1,2}(\mathbf{r}_1, t_k) & \ldots & \Phi_{1,N}(\mathbf{r}_1, t_k) & \ldots & \Phi_{M,1}(\mathbf{r}_1, t_k) & \Phi_{M,2}(\mathbf{r}_1, t_k) & \ldots & \Phi_{M,N}(\mathbf{r}_1, t_k) \\ \Phi_{1,1}(\mathbf{r}_2, t_k) & \Phi_{1,2}(\mathbf{r}_2, t_k) & \ldots & \Phi_{1,N}(\mathbf{r}_2, t_k) & \ldots & \Phi_{M,1}(\mathbf{r}_2, t_k) & \Phi_{M,2}(\mathbf{r}_2, t_k) & \ldots & \Phi_{M,N}(\mathbf{r}_2, t_k) \\ \vdots & \vdots & \ddots & \vdots & \ddots & \vdots & \vdots & \ddots & \vdots \\ \Phi_{1,1}(\mathbf{r}_Q, t_k) & \Phi_{1,2}(\mathbf{r}_Q, t_k) & \ldots & \Phi_{1,N}(\mathbf{r}_Q, t_k) & \ldots & \Phi_{M,1}(\mathbf{r}_Q, t_k) & \Phi_{M,2}(\mathbf{r}_Q, t_k) & \ldots & \Phi_{M,N}(\mathbf{r}_Q, t_k) \end{bmatrix} \tag{18}$$

$$\mathbf{F} = [\ F_1(\omega_1)\ \ F_1(\omega_2)\ \ \ldots\ \ F_1(\omega_N)\ \ \ldots\ \ F_M(\omega_1)\ \ F_M(\omega_2)\ \ \ldots\ \ F_M(\omega_N)\ ]^T \tag{19}$$

With known $\mathbf{e}_{rk}$ and $\mathbf{\Phi}_k$, the result of spectrum vector $\mathbf{F}$ is achieved by utilizing least squares (LS) method as

$$\mathbf{F} = \left(\mathbf{\Phi}_k^T \cdot \mathbf{\Phi}_k\right)^{-1} \cdot \mathbf{\Phi}_k^T \cdot \mathbf{e}_{rk} \tag{20}$$

When the spectrum vector $\mathbf{F}$ is known, the signal of each transmitting element can be obtained by Eq. (13). And the approximate ORF sample $E_r(\mathbf{r}, t_k)$ can be calculated by Eq. (3) or (14).

4. NUMERICAL SIMULATIONS

In this section, numerical experiments are performed to validate the performance of the proposed scheme. Assume that the 5×5 uniform spacing 2-D array with spacing $d = 1\,\mathrm{m}$ is located on the XOY plane.

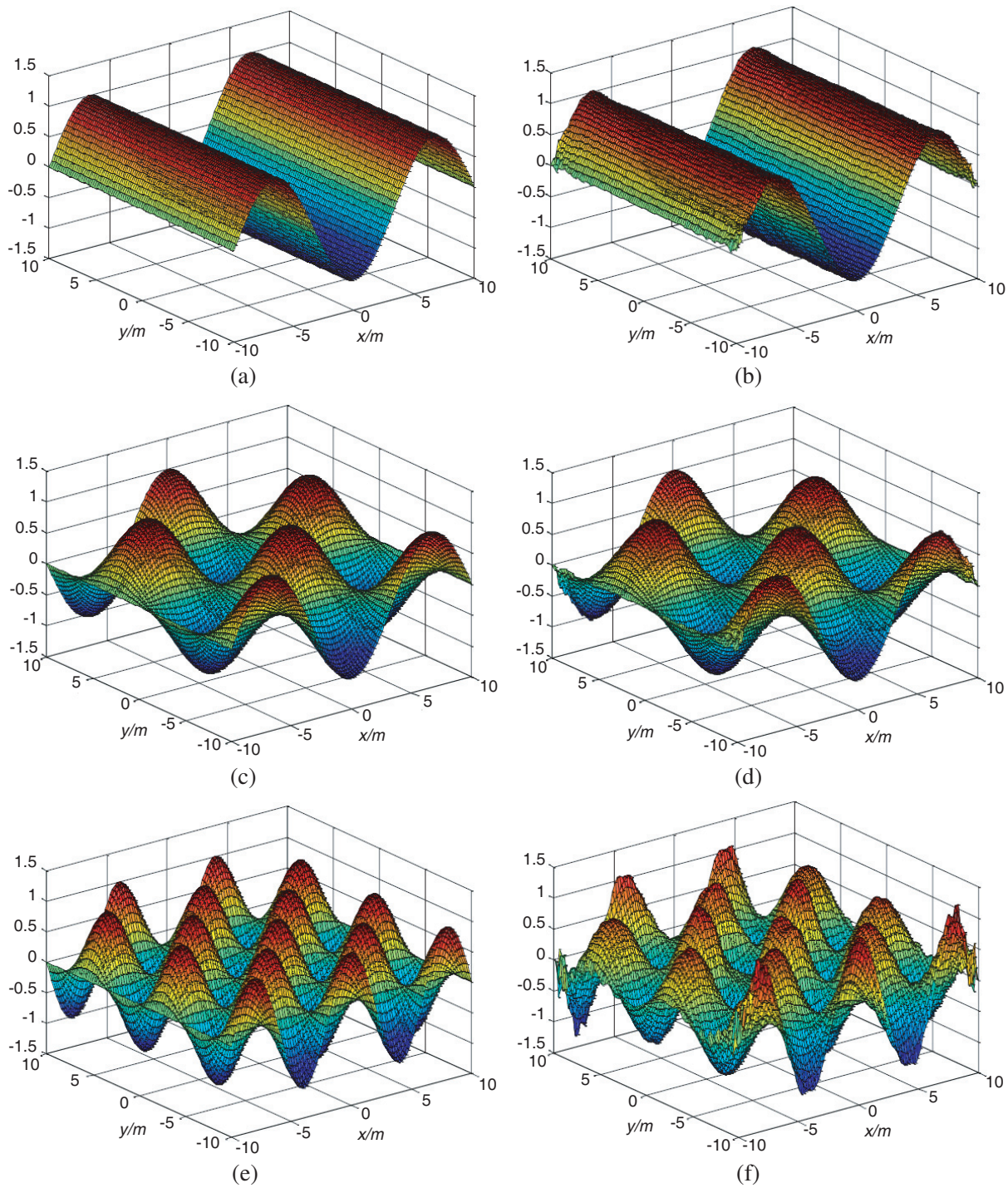

Figure 2. Radiation field samples approximate to different orthogonal basis functions. (a) Orthogonal basis ($i = 3$, $j = 0$). (b) Radiation field ($i = 3$, $j = 0$). (c) Orthogonal basis ($i = 3$, $j = 3$). (d) Radiation field ($i = 3$, $j = 3$). (e) Orthogonal basis ($i = 5$, $j = 5$). (f) Radiation field ($i = 5$, $j = 5$).

The receiver is located at the origin O. The distance between the array center and the imaging region center is 100 m. In the experiments, the imaging region is 20 m × 20 m.

4.1. Orthogonal Radiation Field Approximation

The 2-D orthogonal basis functions are chosen as

$$\Psi_{i,j}(x,y) = \sin\left(\frac{i\pi x}{L_x}+\frac{\pi}{2}\right)\cos\left(\frac{j\pi x}{L_y}+\frac{\pi}{2}\right) \tag{21}$$

where $x \in [-L_x/2, L_x/2]$, $y \in [-L_y/2, L_y/2]$, $i = 1, 2, \ldots, I$, $j = 0, 1, 2, \ldots, J$. According to the simulation parameters, $L_x = L_y = 20\,\mathrm{m}$.

The bandwidth of the signals is limited to 1 GHz, which has the center frequency of 1 GHz. 100 frequency points with uniform spacing are used to synthesize the signals. Therefore, the vector $\mathbf{F}$ has $2500\,(M \times N = 25 \times 100)$ unknowns. Here, the imaging region S is discretized into

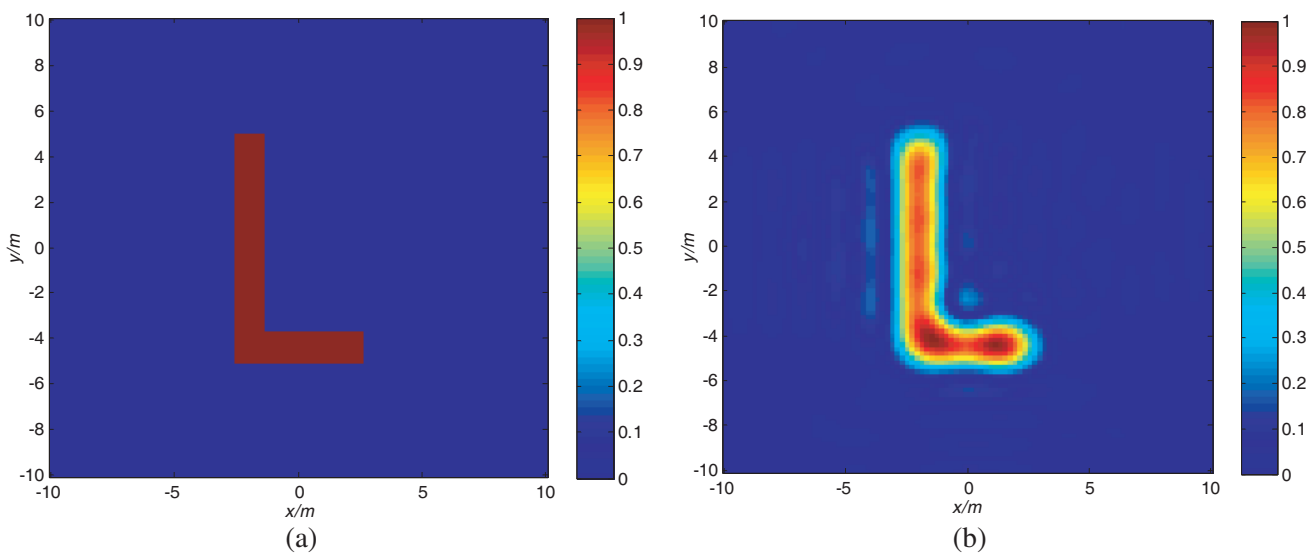

Figure 3. Imaging target and imaging result based on orthogonal radiation field. (a) Imaging target model. (b) Imaging result with no noise.

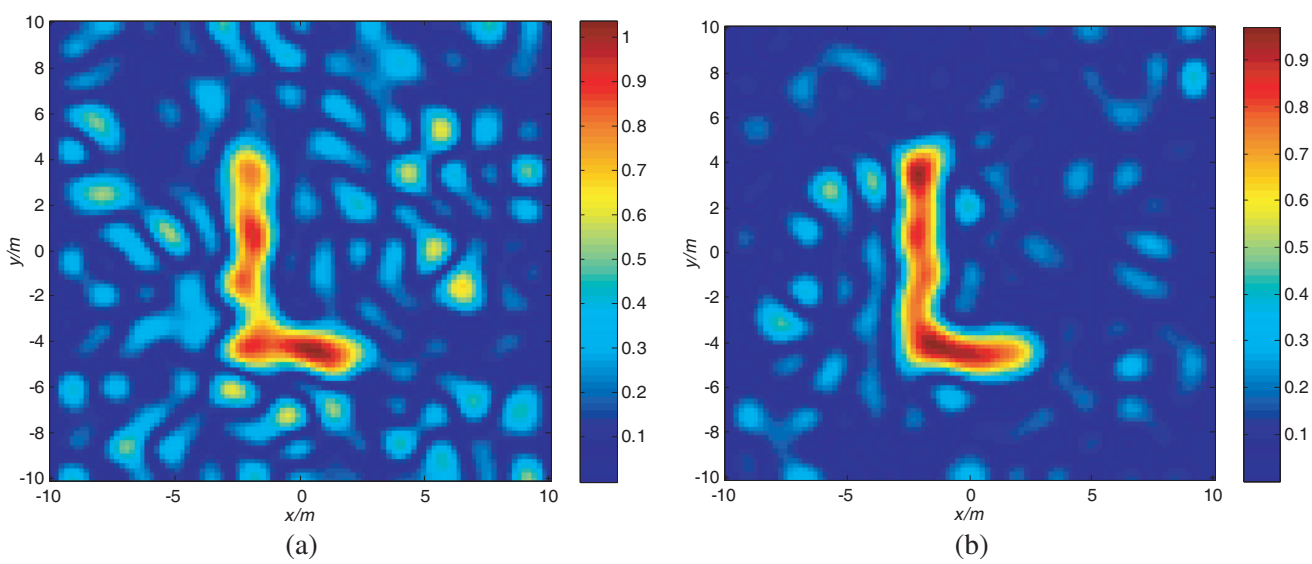

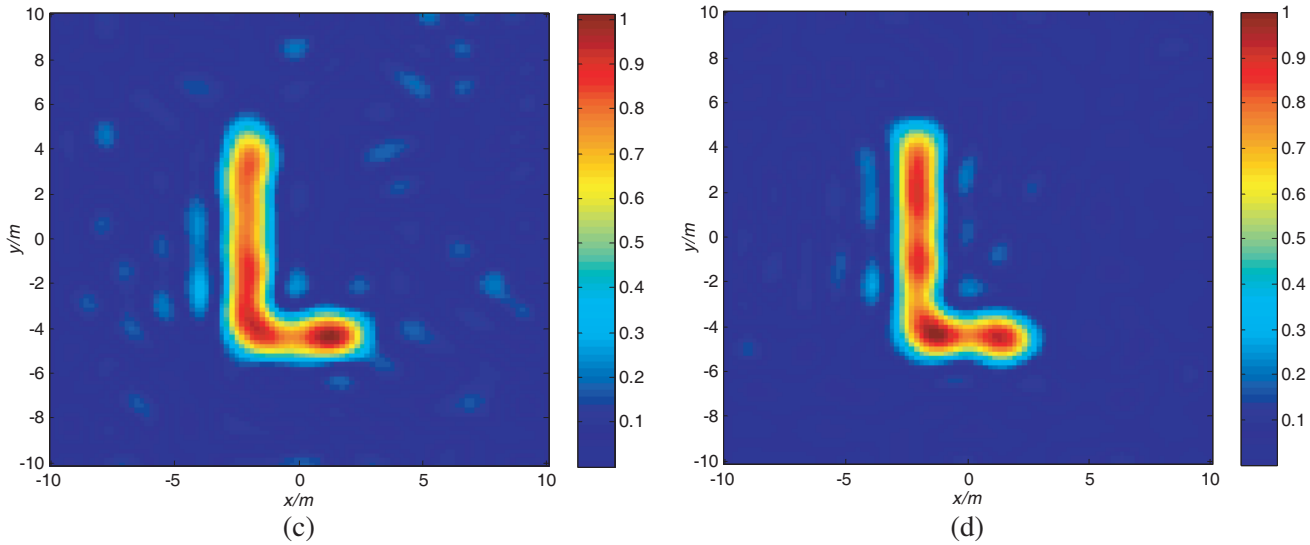

Figure 4. Imaging results with different SNRs based on orthogonal radiation field. (a) Imaging result with SNR = 0 dB. (b) Imaging result with SNR = 5 dB. (c) Imaging result with SNR = 10 dB. (d) Imaging result with SNR = 15 dB.

$100 \times 100\,(Q = 1 \times 10^4)$ cells. It means that an ORF sample provides 1×10^4 spatial sampling values, which is much bigger than the required number to resolve the unknowns in $\mathbf{F}$. The results of the constructed ORF samples are shown in Figure 2.

Figure 2 shows that the ORF samples can be constructed using the method proposed in this paper. However, with the increasing of i and j, and the orthogonal basis function becomes more and more complex as shown in Figures 2(a), (c), (e). Figures 2(b), (d), (f) show that the error of the ORF samples constructed by designing the transmitting signals increases as well. The root mean square error (RMSE) is used to describe the error between the constructed ORF samples and the orthogonal basis functions. And the errors of results shown in Figures 2(b), (d), (f) are 0.0155, 0.0222, and 0.1019 respectively.

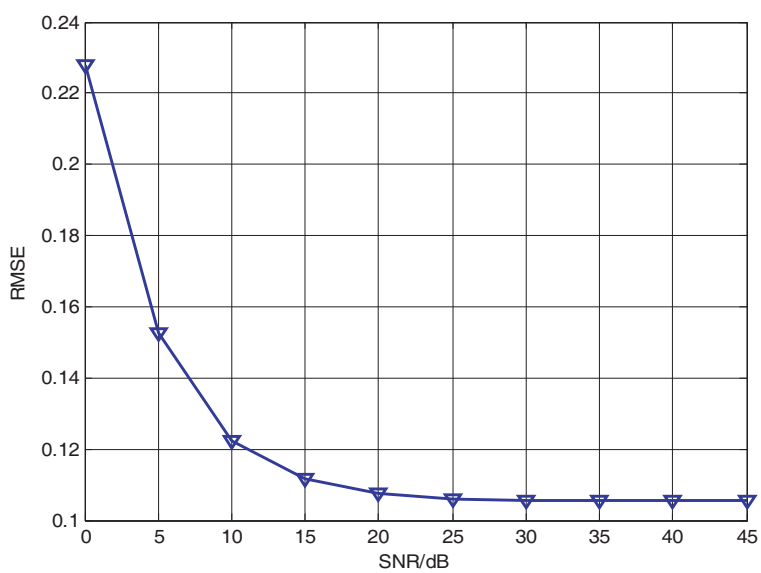

Figure 5. RMSE versus SNR.

4.2. Imaging Based on Orthogonal Radiation Field

The target model is shown in Figure 3(a). Here the imaging region S is discretized into 100×100 cells to reconstruct the target. Due to the limitation of simulation parameters, such as the bandwidth, array size and number of transmitting elements, $240\,(I = 15, J = 15)$ ORF samples are constructed to use in the imaging experiment. Utilizing the pseudo-inverse method, the imaging result with no noise is shown in Figure 3(b). We can see from the imaging result that the shape of the target is successfully reconstructed. According to the traditional radar resolution formula $\Delta\rho = R\lambda/D$, it is about 7.5 m under the parameters in the experiment. Therefore, the imaging result based on ORF has achieved a high resolution reconstruction.

Furthermore, considering the additive noise, the imaging results with different SNRs are shown in Figure 4. It can be seen that with the increase of SNR, the imaging quality becomes better. Moreover, a good imaging performance can be achieved when SNR = 10 dB. It shows that the imaging based on the ORF has better robustness to noise. Figure 5 shows that the imaging error varies with SNR. With the increase of SNR, the imaging error decreases rapidly at the beginning, and then it tends to be constant

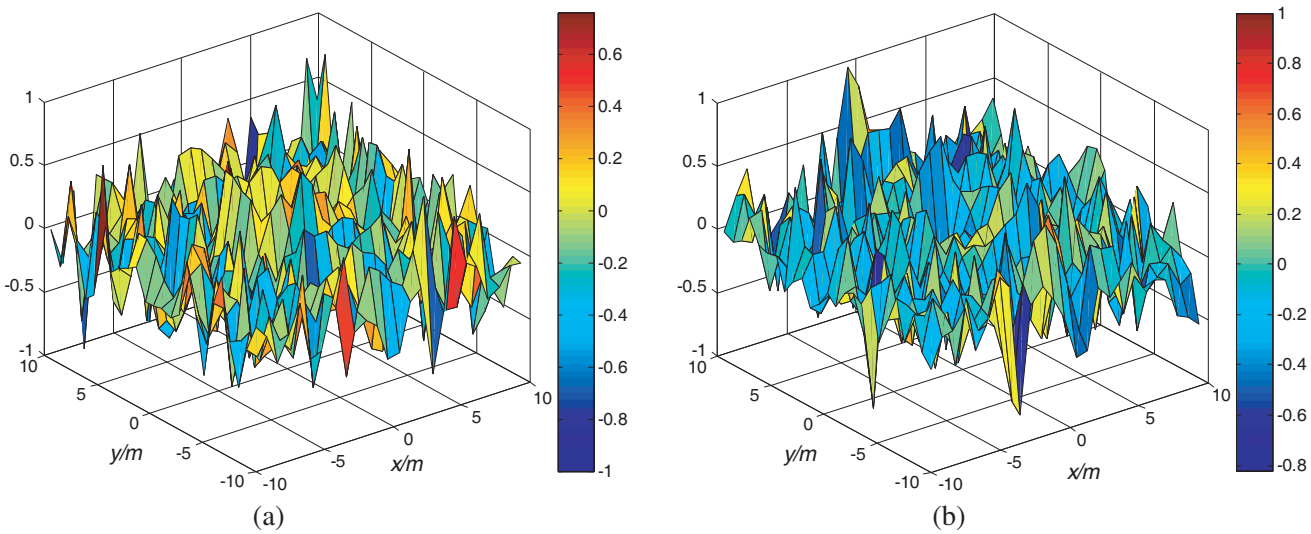

Figure 6. The ordinary temporal-spatial independent radiation field samples. (a) Sample 1. (b) Sample 2.

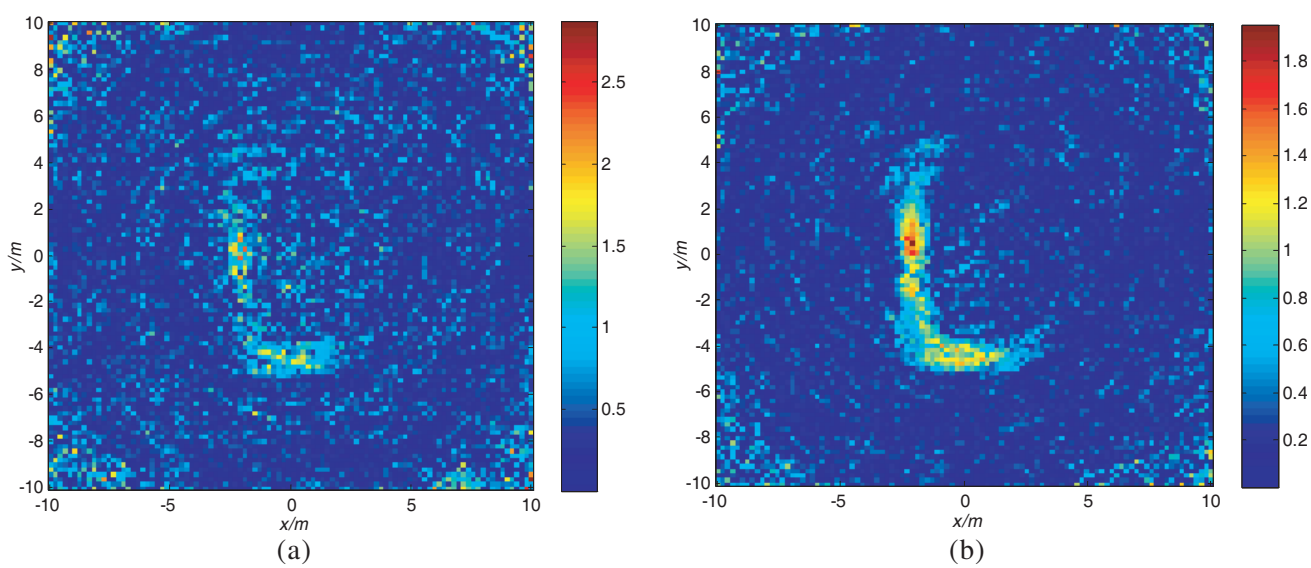

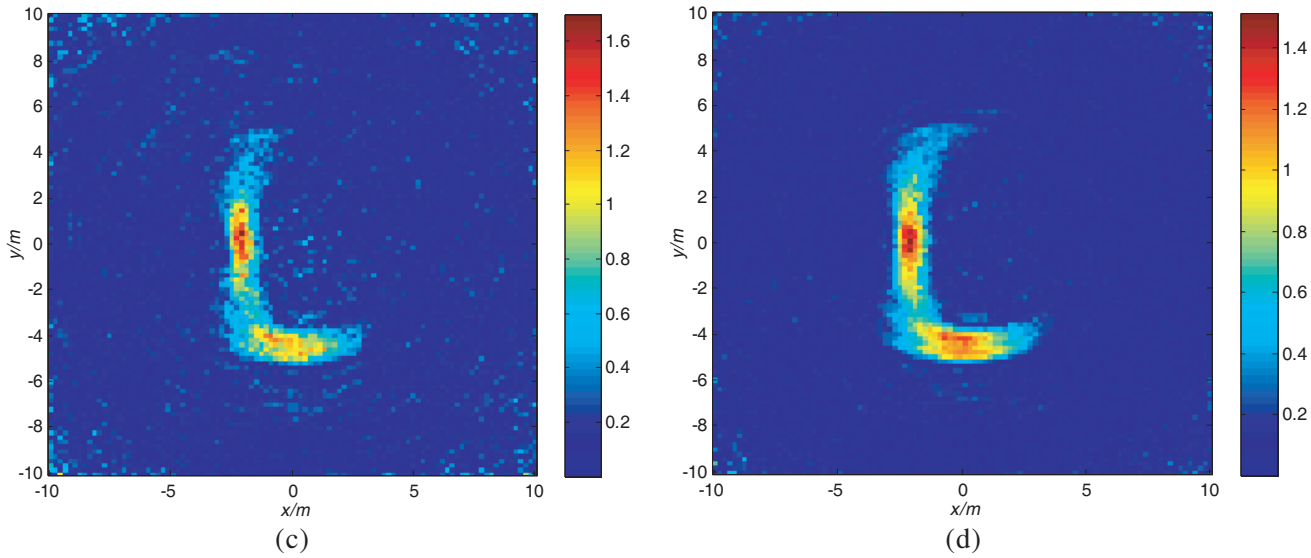

Figure 7. Imaging results with different SNRs based on the ordinary temporal-spatial independent radiation field. (a) Imaging result with SNR = 0 dB. (b) Imaging result with SNR = 5 dB. (c) Imaging result with SNR = 10 dB. (d) Imaging result with SNR = 15 dB.

when the SNR is greater than 20 dB. It means that the effect of noise can be ignored when the SNR is greater than 20 dB.

4.3. Comparison

In this section, with the same simulation parameters, an imaging experiment based on the ordinary temporal-spatial independent radiation field is performed to compare with the proposed method. Herein, the signals are chosen to be bandpass white Gaussian noise. Then, the ordinary temporal-spatial independent radiation field samples can be derived from Eq. (3), as shown in Figure 6. Figure 7 shows

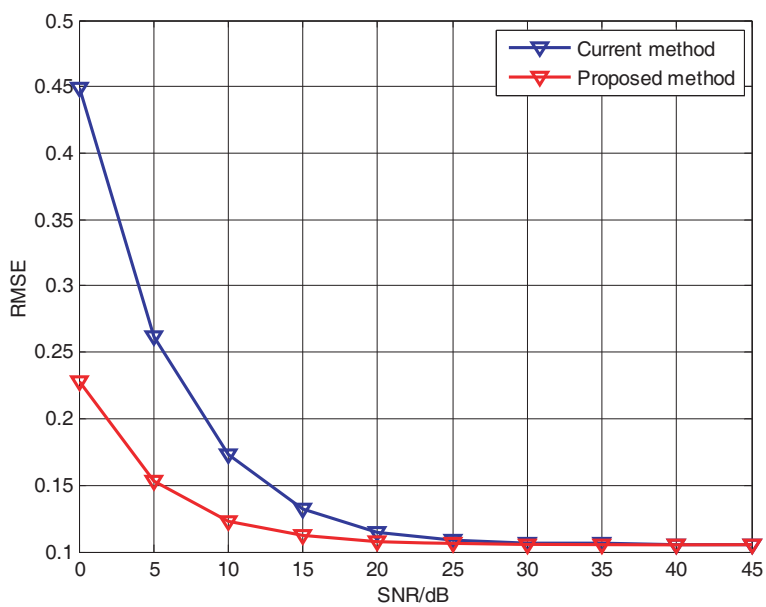

Figure 8. Imaging errors comparison.

the imaging results based on ordinary temporal-spatial independent radiation field with different SNRs. When SNR is 0 dB, it is almost failed to reconstruct the target, as shown in Figure 7(a). And the imaging result is still blurry when SNR is 5 dB, as shown in Figure 7(b). Figure 7(d) shows a result that we can see the shape of the target, but the backscattering coefficient distribution of the target is not uniform as the target model shown in Figure 3(a).

Comparing Figure 7 with Figure 4, it is obvious that the imaging results based on ORF are much better when SNR is the same. And it is also verified by comparison of imaging errors shown in Figure 8.

5. CONCLUSIONS

In this paper, we present a novel kind of ideal independent radiation field named the orthogonal radiation field for MSCI. It is an inverse method to construct the independent radiation field. It means that the ORF samples are supposed to exist firstly, and then they can be constructed by properly designing the transmitting signals. When the ORF is applied in MSCI, the imaging model is robust to noise while the row vectors of the imaging matrix are approximately orthogonal. Therefore, we can achieve better imaging performance when the SNR is low. Simulation results demonstrate the feasibility of the ORF samples construction. Compared with current imaging scheme based on ordinary temporal-spatial independent radiation field, the proposed imaging scheme based on ORF is validate to have superior performance in different SNR situations.

REFERENCES

1. Guo, Y., D. Wang, and X. He, "A novel super-resolution imaging method based on stochastic radiation radar array," *Measurement Science and Technology*, Vol. 24, No. 7, 074013, Jun. 2013.
2. Ma, Y., X. He, and D. Wang, "Microwave staring correlated imaging and resolution analysis," *Geo-Informatics in Resource Management and Sustainable Ecosystem International Symposium (GRMSE 2013)*, 737–747, Nov. 2013.
3. Li, D., X. Li, Y. Cheng, Y. Qin, and H. Wang, "Radar coincidence imaging: An instantaneous imaging technique with stochastic signals," *IEEE Transactions on Geoscience Remote Sensing*, Vol. 52, No. 4, 2261–2271, Apr. 2014.
4. Zhu, S., A. Zhang, Z. Xu, et al., "Radar coincidence imaging with random microwave source," *IEEE Antennas and Wireless Propagation Letters*, Vol. 14, 1239–1242, 2015.
5. Li, D., X. Li, Y. Cheng, et al., "Three dimensional radar coincidence imaging," *Progress In Electromagnetics Research M*, Vol. 33, 223–238, 2013.
6. Guo, Y., D. Wang, and C. Tian, "Research on sensing matrix characteristics in microwave staring correlated imaging based on compressed sensing," *2014 IEEE International Conference on Imaging Systems and Techniques (IST)*, 195–200, IEEE, 2014.
7. Li, D., X. Li, Y. Cheng, et al., "Radar coincidence imaging under grid mismatch," *ISRN Signal Processing 2014*, 2014.
8. Zhou, X., H. Wang, Y. Cheng, et al., "Radar coincidence imaging for off-grid target using frequency-hopping waveforms," *International Journal of Antennas and Propagation 2016*, 2016.
9. Zha, G., H. Wang, Z. Yang, et al., "Effect analysis and design on array geometry for coincidence imaging radar based on effective rank theory," *2015 ISPRS International Conference on Computer Vision in Remote Sensing*, International Society for Optics and Photonics, 2016.
10. Yang, H., L. Zhang, Y. Gao, et al., "Azimuth wavefront modulation using plasma lens array for microwave staring imaging," *2015 IEEE International Geoscience and Remote Sensing Symposium (IGARSS)*, 4276–4279, IEEE, 2015.
11. Fromenteze, T., O. Yurduseven, M. F. Imani, et al., "Computational imaging using a mode-mixing cavity at microwave frequencies," *Applied Physics Letters*, Vol. 106, No. 19, 194104, 2015.
12. Yurduseven, O., V. R. Gowda, J. N. Gollub, et al., "Printed aperiodic cavity for computational and microwave imaging," *IEEE Microwave and Wireless Components Letters*, Vol. 26, No. 5, 367–369, 2016.

13. Hunt, J., J. Gollub, T. Driscoll, et al., "Metamaterial microwave holographic imaging system," *JOSA A*, Vol. 31, No. 10, 2109–2119, 2014.
14. Watts, C. M., D. Shrekenhamer, J. Montoya, et al., "Terahertz compressive imaging with metamaterial spatial light modulators," *Nature Photonics*, Vol. 8, No. 8, 605–609, 2014.